

## Article

# Microstructure and Hydrogen Storage Performance of Ball-Milled $\text{MgH}_2$ Catalyzed by FeTi

Ádám Révész <sup>1,\*</sup>, Roman Paramonov <sup>1</sup>, Tony Spassov <sup>2</sup> and Marcell Gajdics <sup>1,3</sup><sup>1</sup> Department of Materials Physics, Eötvös Loránd University, H-1518 Budapest, Hungary<sup>2</sup> Department of Chemistry, University of Sofia “St. Kl. Ohridski”, 1164 Sofia, Bulgaria<sup>3</sup> Center of Energy Research, Hungarian Academy of Sciences, H-1121 Budapest, Hungary

\* Correspondence: revesz.adam@ttk.elte.hu

**Abstract:** A high-energy ball-milling method was applied for different milling times (1 h, 3 h, and 10 h) to synthesize nanocrystalline  $\text{MgH}_2$  powder samples catalyzed by  $\text{Fe}_2\text{Ti}$ . Morphology and microstructure of the powders were characterized by scanning electron microscopy and X-ray diffraction. The recorded diffraction profiles were evaluated by the convolutional multiple whole profile fitting algorithm, in order to determine microstructural parameters of the composites, such as average crystallite size and average dislocation density. Differential scanning calorimetry was performed to investigate the dehydrogenation characteristics of the alloys. It was obtained that there exists an optimal milling time (3 h) when desorption occurs at the lowest temperature. X-ray diffraction of partially dehydrided states confirmed a two-step H-release, including the subsequent desorption of  $\gamma\text{-MgH}_2$  and  $\alpha\text{-MgH}_2$ . The effect of milling time on the H-sorption performance was investigated in a Sievert-type apparatus. The best overall hydrogenation performance was obtained for the composite milled for 3 h.

**Keywords:** ball-milling; magnesium; FeTi catalyst; hydrogen storage



**Citation:** Révész, Á.; Paramonov, R.; Spassov, T.; Gajdics, M. Microstructure and Hydrogen Storage Performance of Ball-Milled  $\text{MgH}_2$  Catalyzed by FeTi. *Energies* **2023**, *16*, 1061. <https://doi.org/10.3390/en16031061>

Academic Editor: Andrzej Teodorczyk

Received: 23 December 2022

Revised: 12 January 2023

Accepted: 16 January 2023

Published: 18 January 2023



**Copyright:** © 2023 by the authors. Licensee MDPI, Basel, Switzerland. This article is an open access article distributed under the terms and conditions of the Creative Commons Attribution (CC BY) license (<https://creativecommons.org/licenses/by/4.0/>).

## 1. Introduction

Continuous population development and growth have led to drastically increased energy consumption in the last couple of decades. The majority of modern energy sources are still non-renewable, resulting in exhaustive  $\text{CO}_2$  emission [1]. In addition, the availability of fossil resources will be limited in the near future. As a consequence, renewable sources have rapidly gained popularity even though a lot of technological and economical challenges are yet to be solved [2,3]. The unpredictability of some renewable sources and location-locked positioning of others generate some problems for transportation of this energy to the grid. A numerous sources consider hydrogen as a potential solution for these problems due to its exceptionally high chemical energy density, environmental cleanness and harmless reactions [4].

Lately, worldwide intensive research has been targeting hydrogen storage in the solid state with sufficient H-capacity [5–8]. Among different elements and compounds, magnesium and its alloys are some of the most investigated systems, because of their high hydrogen absorption capacity (7.6 wt.%, or 2600 Wh/kg), low mass density, relatively low cost and non-toxicity, which may lead to future industrial applications of these materials [9–12]. Nonetheless, commercial magnesium also possesses poor thermodynamics, sluggish kinetics below 300 °C and high hydrogenation enthalpy which generally make this material practically inapplicable at the moment.

Numerous investigations have been carried out recently in order to improve the kinetic performance and temperature of H-sorption of Mg-based systems, including nanocrystallization by a top-down approach and catalyst addition. Application of high-energy ball-milling (HEBM) [13,14] can reduce the average crystallite size of magnesium down

to nanometric dimensions and induce severe plastic deformation (SPD) which drastically improves sorption kinetics due to the increased volume fraction of grain boundaries [15–18]. In addition, the abundant lattice defects generated during HEBM within the individual powder particles can further improve the hydrogen sorption kinetics due to the enhanced diffusion length of hydrogen [19,20].

Besides nanocrystallization, the kinetics and cyclic life of  $\text{MgH}_2$  and Mg-based materials can be further improved by different additives. Among these catalysts, transition metals (Ni, Fe) [21–25], transition metal oxides ( $\text{Fe}_2\text{O}_3$ ,  $\text{TiO}_2$  and  $\text{Nb}_2\text{O}_5$ ) [26–29] and carbon-based materials [30–32] are the most common. Such a catalytic effect apparently is caused by significant reduction of hydride formation enthalpy supported through promotion of hydrogen molecule dissociation at the surface [10,23].

FeTi, as a combination of two transition metal elements, has gained noticeable attention since nanocrystalline Mg-FeTi composites were reported to have an outstanding hydrogenation performance. For example, arc melting of FeTi and mixing with Mg by HEBM results in appropriately fast kinetics at elevated temperatures. The hydriding and dehydriding rate of this  $\text{MgH}_2$ -35 wt.% FeTi<sub>1.2</sub> composite increases with milling time, however, longer processing time results in the degradation of H-storage capacity [33]. When a substantial amount of FeTi catalyst was ball-milled to  $\text{MgH}_2$ , the nanocrystalline  $\text{MgH}_2$ -x wt.% FeTi (x = 40, 50, 60) series exhibited detectable hydrogen absorption performance even at room temperature. It was established that the  $\text{MgH}_2$ -40 wt.% FeTi alloy milled for 36 h showed the best overall absorption capacity, i.e., it was able to absorb 3 wt.% of hydrogen in 1 h [34]. As a continuation of this research, the effect of milling conditions on hydrogenation sorption properties of  $\text{MgH}_2$ -40 wt.% FeTi was investigated. Accordingly, a better FeTi microstructural refinement and distribution can be achieved by applying protective media during milling (such as wet milling), which can significantly increase the hydrogen capacity of this composite [35]. In order to achieve proper hydrogenation kinetics at room temperature in the Mg-TiFe<sub>0.92</sub>Mn<sub>0.08</sub> system, it is essential to mix at least 50 wt.% of FeTi additive with magnesium hydride by HEBM. On the other hand, the rate of hydrogen uptake becomes similarly rapid for all applied catalyst amounts (20, 35 and 50 wt.%) at elevated temperatures up to 350 °C [36]. In recent research, it was demonstrated that when Mg was catalyzed not only by FeTi, but with the addition of carbon nanotubes, the hydrogenation kinetics were exceptionally fast, reaching 6.6 wt.% absorbed  $\text{H}_2$  in 1 min at 150 °C [37]. A detailed analysis on the H-performance of nanocrystalline  $\text{MgH}_2$  catalyzed only by Fe revealed the importance of the processing parameters by HEBM and the optimal concentration of the catalyst [38].

In addition, the FeTi system itself is able to absorb and desorb hydrogen. For example, SPD of nanostructured FeTi compound obtained by gas atomization can promote full absorption [39]. Doping FeTi by Zr, Mn or Y additives promotes the activation of hydrogen uptake at room temperature, however, with a sluggish kinetics [40–42]. When FeTi alloy is subjected to SPD by different processing routes, such as HEBM, high-pressure torsion and groove or cold rolling, the formation of cracks and subgrain boundaries positively influence the activation of hydrogenation [43–46].

In the current research, 10 wt.% Fe<sub>2</sub>Ti intermetallic powder with a stoichiometric composition was mixed with  $\text{MgH}_2$  and subjected to HEBM for different milling times. In order to achieve a proper catalytic effect of the additive, the FeTi mixture was activated first in the ball-mill and then properly dispersed among the  $\text{MgH}_2$  particles by prolonged milling times. The work demonstrated the effect of the FeTi catalyst and preparation conditions on the microstructural evolution, morphology and hydrogenation/dehydrogenation performance of  $\text{MgH}_2$ .

## 2. Materials and Methods

### 2.1. Sample Preparation

As an initial step, nanocrystalline FeTi catalysts were prepared by high-energy ball-milling (HEBM) of elemental Fe and Ti powders (purity 99.9%) in a 2:1 stoichiometric ratio

using a SPEX 8000M Mixer Mill operating at 1425 RPM. For each milling, a stainless steel vial (volume: 65 mL) containing 10 stainless steel balls (1/4 in.) was applied, thus the ball-to-powder weight ratio was set as 10:1. Based on our previous studies [47], two pre-milling times (3 h and 10 h) were selected to achieve good homogeneity of the catalyst powders, these samples will be denoted as FeTi (3 h) and FeTi (10 h), respectively. Thereafter, the FeTi (10 h) catalyst was further milled to the MgH<sub>2</sub> powder (5 wt.% Mg in balance, Sigma-Aldrich, St. Louis, MA, USA) in a 1:9 mass ratio to obtain 1 g of MgH<sub>2</sub>-FeTi composite mixture. The 10 wt.% catalyst concentration seems to be an optimal value, since lower amounts are insufficient to avoid poorly catalyzed regions, while higher concentrations may not improve the H-kinetics further [38]. The HEBM procedure was conducted for 3 different milling times of 1 h, 3 h and 10 h, obtaining MgH<sub>2</sub>/FeTi (1 h), MgH<sub>2</sub>/FeTi (3 h) and MgH<sub>2</sub>/FeTi (10 h) powder blends, respectively. The entire powder synthesis procedure was carried out in a protective Ar atmosphere. For longer milling times, the milling procedure was interrupted after each hour and the vial was rotated by 90 deg along its symmetrical axis in order to achieve homogeneous powders.

## 2.2. Microstructural Characterization

### 2.2.1. X-ray Diffraction

The microstructure of the FeTi catalyst powders and MgH<sub>2</sub>/FeTi composites was investigated by X-ray powder diffraction (XRD). All measurements were carried out on a Rigaku SmartLab diffractometer in  $\theta$ -2 $\theta$  geometry using Cu-K $\alpha$  radiation. The data were collected in Bragg-Brentano geometry in the range from 20° to 75° with a step size of 0.01°. For further microstructural analysis, the recorded XRD patterns were analyzed by the convolutional multiple whole profile (CMWP) fitting method [48]. In brief, this analysis incorporates the direct fit of the whole measured diffractogram by the sum of theoretically constructed profile functions, background and measured instrumental profiles [49]. The applied profile functions are generated for each Bragg reflection of each crystalline phase as the inverse Fourier transform of the product of the size and strain Fourier coefficients providing both strain and size parameters of the microstructure. Accordingly, the average coherently scattering domain size or crystallite size can be given as

$$D = m \exp(3.5 \sigma^2), \quad (1)$$

where  $\sigma$  and  $m$  are the variance and median of the lognormal size distribution of the crystallite size, respectively. The most important strain parameter determined from the CMWP algorithm is the average dislocation density ( $\rho$ ) [49]. Details of the model can be found elsewhere [48,49] and its applicability on exploring the microstructural evolution of hydrogen storage materials is justified in several recent publications [18,47,50].

### 2.2.2. Scanning Electron Microscopy

Surface morphology of the as-milled powder composites was characterized by a tabletop Hitachi TM4000Plus scanning electron microscope (SEM) using back-scattered electron (BSE) and secondary electron (SE) regimes. Particle sizes for the hydride samples were determined by ImagePro+ using a linear intercept method based on 50 counts. Energy-dispersive X-ray spectroscopy (EDS) analysis was also applied to determine the chemical composition of powder blends. All measurements were carried out at 15 kV of accelerating voltage.

## 2.3. Thermal Characterization

Linear heating scans were performed on a power-compensated Perkin Elmer differential scanning calorimeter (DSC) at a heating rate of 40 K min<sup>-1</sup> in the temperature range of 320–950 K. Measurements were carried out under high-purity Ar flux. The MgH<sub>2</sub>/FeTi powders were placed in Al sample holders. Temperature and enthalpy were calibrated by the melting of pure In and Al.

#### 2.4. Hydrogen Storage Experiments

The hydrogen storage properties of the samples were investigated using a home-made Sieverts-type apparatus. Isothermal absorption and desorption measurements were performed at 573 K, with an initial hydrogen pressure of 1 MPa and 1 kPa, respectively. The actual measurements were carried out after a full hydrogenation–dehydrogenation activation cycle. For each experiment, ~80–90 mg of powder was used.

### 3. Results and Discussion

#### Characterization of the As-Milled Powders

Figure 1 represents the XRD patterns of the un-milled FeTi powder blend (FeTi (mix)), the as-milled FeTi (3 h) and FeTi (10 h) catalysts. It is evident from the patterns that Ti is consumed totally during the HEBM procedure, while the formation of a FeTi solid solution ( $\text{Fe}_{0.975}\text{Ti}_{0.025}$ ) takes place after 3 h of milling. The lack of Ti Bragg peaks confirms that titanium atoms occupy positions in the Fe lattice. In addition, prolonged millings up to 10 h shows some hints of an  $\text{Fe}_2\text{Ti}$  intermetallic phase. Based on these preliminary results, the FeTi (10 h) powder was chosen as an additive by HEBM to commercial  $\text{MgH}_2$ .

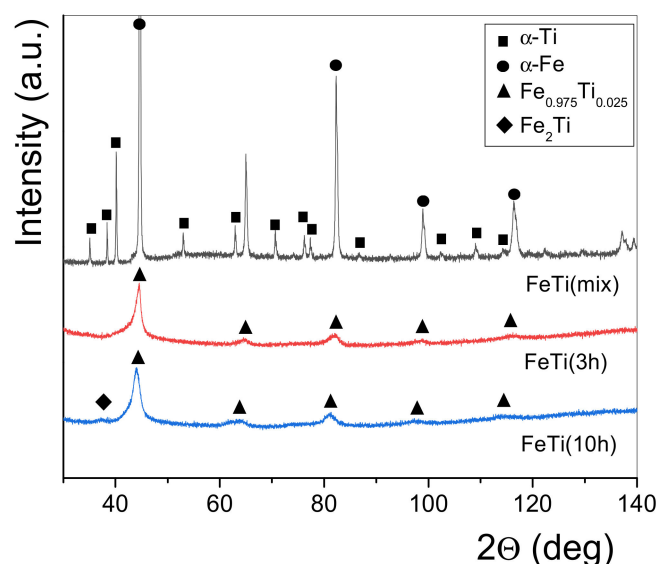


**Figure 1.** X-ray diffraction patterns for the FeTi (mix), FeTi (3 h) and FeTi (10 h) catalyst powders.

As a common feature of the scanning electron micrographs, all the as-milled  $\text{MgH}_2/\text{FeTi}$  composite powders contain agglomerates with different particle sizes (Figure 2a,c,e). Some of these agglomerates possess flat surfaces which may develop during the powder–vial and powder–ball collisions, when the initially soft powder particles stick to the hard surfaces. Nevertheless, as one can notice, the  $\text{MgH}_2/\text{FeTi}$  (10 h) powder is less abundant in flattened agglomerates, which may correspond to the intensive homogenization of the powder particles that occurred during SPD by HEBM. Quantitative analysis of the SEM micrographs revealed that the average powder particle size is ~2  $\mu\text{m}$ , independently of the applied milling time. This characteristic value is in accordance with other HEBM-treated Mg-based hydrogen storage powders [20,38].

Brighter spots on the enlarged BSE images of the  $\text{MgH}_2/\text{FeTi}$  composites correspond to FeTi catalyst particles homogeneously dispersed among the hydride agglomerates or pressed into their surface (Figure 2b,d,f). As seen, the catalyst agglomerates are significantly smaller in size. The corresponding EDS spectra are presented as insets of Figure 2 and the elemental analysis confirmed that all powders are dominated by Mg with an average of 92–94 wt.%. At the same time, the overall concentration of the FeTi catalyst is lower than the nominal value for all the composites (6.02 wt.% for  $\text{MgH}_2/\text{FeTi}$  (1 h), 8.20 wt.% for  $\text{MgH}_2/\text{FeTi}$  (3 h) and 8.54 wt.% for  $\text{MgH}_2/\text{FeTi}$  (10 h)). This discrepancy can be explained



by the different mechanical properties of the  $\text{MgH}_2$  and FeTi powders, namely, the catalyst powder particles may stick and/or adhere to the edges and walls of the milling container. The lowest measured catalyst content for the  $\text{MgH}_2/\text{FeTi}$  (1 h) alloy may be related to the lack of homogeneous catalyst distribution and absence of vial rotation procedures which were performed for other samples after each hour.

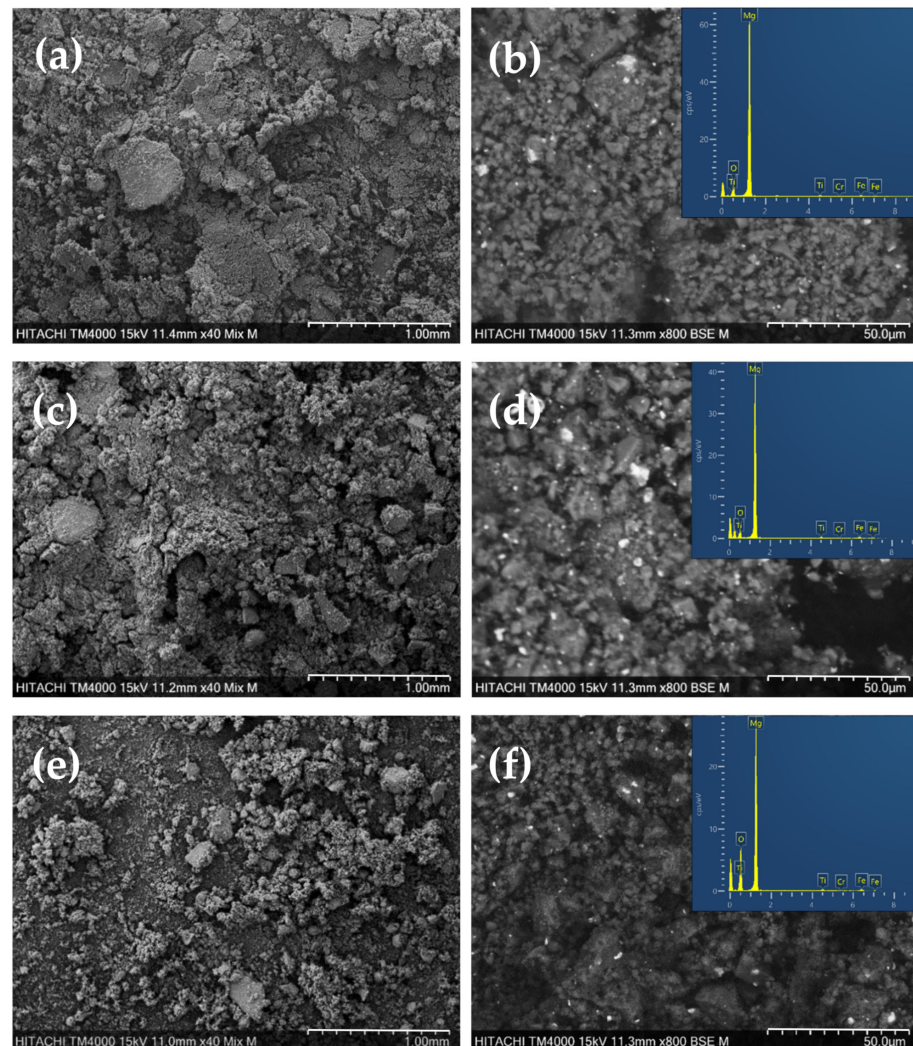


**Figure 2.** Low-magnification (BSE + SE) and high-magnification (BSE) SEM images for (a,b)  $\text{MgH}_2/\text{FeTi}$  (1 h), (c,d)  $\text{MgH}_2/\text{FeTi}$  (3 h) and (e,f)  $\text{MgH}_2/\text{FeTi}$  (10 h) composites. Insets show the corresponding EDS spectra.

The XRD patterns of the as-milled  $\text{MgH}_2/\text{FeTi}$  powder composites are plotted in Figure 3. As seen, all patterns are dominated by the reflections of tetragonal  $\alpha\text{-MgH}_2$ , however, the high-pressure  $\gamma\text{-MgH}_2$  phase is also present for each powder. As one can also notice, the  $\text{MgH}_2/\text{FeTi}$  (1 h) composite contains some hexagonal Mg, originating from the commercial  $\text{MgH}_2/\text{Mg}$  powder, which gradually disappears with increasing milling time. At the same time, a broad peak of MgO at  $2\theta = 44$  deg is present for all the  $\text{MgH}_2/\text{FeTi}$  powders, however, its intensity remains practically unchanged with increasing milling time. The Bragg peaks of  $\alpha\text{-MgH}_2$  are significantly reduced in height and increased in width due to the SPD that occurred during HEBM, resulting in an intensive crystallite size reduction and lattice defect generation [20]. It is also noted that no reflections of the FeTi phase are observed in the patterns, which may be related to the low relative volume fraction of the catalyst and/or to a solid state amorphization [51]. A typical example of the measured and fitted profiles together with the difference plot obtained by the CMWP

analysis are seen in Figure 4. It is undoubted from the figure that the numerical algorithm has satisfactorily converged.

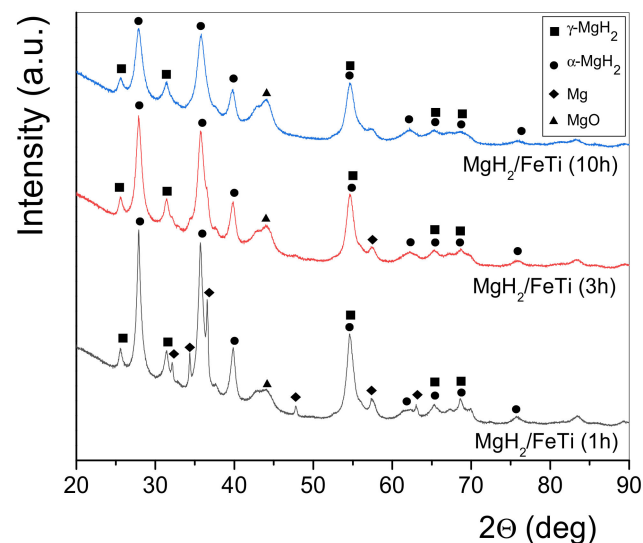


**Figure 3.** XRD patterns of the ball-milled  $\text{MgH}_2/\text{FeTi}$  composite powders.

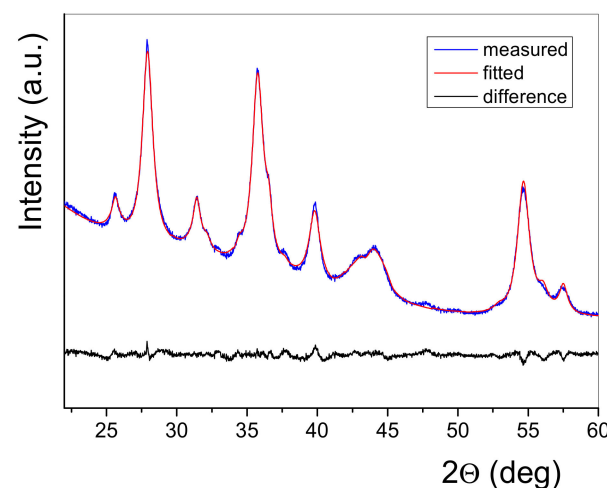


**Figure 4.** XRD profile of the  $\text{MgH}_2/\text{FeTi}$  (3 h) composite powder fitted by the CMWP method. The difference between the measured pattern and the fitted profile is also presented.

By evaluating the XRD line profiles, the average coherently scattered crystallite sizes of the different phases are plotted in Figure 5. In general, the  $D$  values of the  $\alpha\text{-MgH}_2$  and  $\gamma\text{-MgH}_2$  hydride phases are practically constant in the range of 7–12 nm for all milling times, corresponding to a significant nanocrystallization during the HEBM process, which can promote enhanced sorption kinetics of the  $\text{MgH}_2/\text{FeTi}$  system. The crystallite size values of  $\text{MgH}_2$  obtained by the CMWP fitting algorithm are in accordance with the results of a Rietveld analysis carried out on ball-milled  $\text{MgH}_2\text{-Fe}$  [38]. At the same time, the average crystallite size of hexagonal Mg obtained after 1 h of HEBM is significantly larger (31 nm), however, this minor phase plays a less important role with prolonged milling time. The obtained dislocation density for both hydride phases reaches remarkable high values ( $\rho \sim 10^{15} \text{ m}^{-2}$ ), indicating that HEBM is not only able to reduce the coherent crystallite size, but induce a huge number of lattice defects, which can enhance the hydrogen kinetic performance of this system. The highest value ( $\rho = 4.8 \times 10^{15} \text{ m}^{-2}$ ) was achieved for the high-pressure  $\gamma\text{-MgH}_2$  phase in the  $\text{MgH}_2/\text{FeTi}$  (10 h) alloy, which significantly exceeds the defect density obtained for nanocrystalline  $\text{MgH}_2$  without any catalyst [50] and Mg

catalyzed by  $\text{TiO}_2$  [47], indicating that the FeTi catalyst powder particles have a positive effect on the microstructural refinement upon ball-milling. Despite the very high value of  $\rho$ , the calculated average dislocation distance ( $L = \rho^{-1/2} = 14.4 \text{ nm}$ ) of the  $\gamma\text{-MgH}_2$  phase in the  $\text{MgH}_2/\text{FeTi}$  (10 h) powder exceeds the corresponding crystallite size ( $D = 10.2 \text{ nm}$ ), therefore it is concluded that each coherently scattered crystallite contains, on average, less than one dislocation.

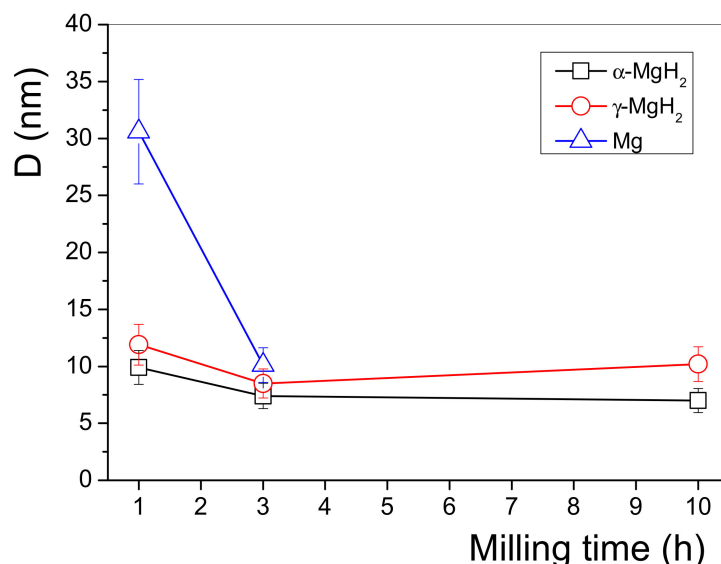


**Figure 5.** Variation of the size of coherently scattered crystallites of the  $\text{MgH}_2/\text{FeTi}$  powders as a function of the milling time.

Figure 6 presents the linear heating calorimetric measurement for all the  $\text{MgH}_2/\text{FeTi}$  composites. It is evident from the thermograms that each scan exhibits a two-step endothermic process, which is related to dehydrogenation of the  $\alpha$  and  $\gamma$  phases completed at  $T_1$  and  $T_2$  temperatures, respectively. The lower  $T_1$  temperature of the  $\alpha - \text{MgH}_2 \rightarrow \text{Mg} + \text{H}_2$  reaction corresponds to the lower stability of Mg-H bonds in this hydride phase. The inset of Figure 6 shows the variation of the onset of the first reaction ( $T_{1,\text{onset}}$ ),  $T_1$  and  $T_2$  as a function of the milling time. It is undoubtedly confirmed that there exists an optimal milling time, i.e., the  $\text{MgH}_2/\text{FeTi}$  (3 h) composite possesses the lowest dehydrogenation stability among all the powders. In our opinion, the lower stability of the  $\text{MgH}_2/\text{FeTi}$  (1 h) and  $\text{MgH}_2/\text{FeTi}$  (3 h) composites might be related to the presence of nanocrystalline Mg originating from the commercial powders (see the XRD patterns in Figure 3). These pre-existing Mg nanocrystallites can promote the growth of the Mg phase at the beginning of the dehydrogenation process without any nucleation. As seen from Figure 5, the average crystallite size of Mg is remarkably smaller for the  $\text{MgH}_2/\text{FeTi}$  (3 h) alloy than for  $\text{MgH}_2/\text{FeTi}$  (1 h), providing larger driving force for the subsequent evolution of the Mg phase.

In order to monitor the phase evolution during dehydrogenation of the  $\text{MgH}_2/\text{FeTi}$  (3 h) composite, a linear heating DSC scan was interrupted at temperatures  $T = 625 \text{ K}$ ,  $T = 650 \text{ K}$ ,  $T = 675 \text{ K}$  and  $T = 700 \text{ K}$ . For comparison, the fully dehydrided state was also obtained after two repetitive heating runs up to  $T = 800 \text{ K}$ . A general view on the effect of hydrogen desorption of  $\text{MgH}_2/\text{FeTi}$  (3 h) can be inferred from a series of XRD patterns carried out on the partial dehydrogenated powders, see Figure 7. As the H-content of the composite is released gradually, the Bragg peaks of the high-pressure  $\gamma\text{-MgH}_2$  phase tends to diminish, while the major  $\alpha\text{-MgH}_2$  hydride phase is present up to  $T = 700 \text{ K}$ . At the same time, the relative intensity of the reflections of a hexagonal Mg phase increases considerably, while the pattern obtained after linear heating up to  $T = 800 \text{ K}$  is characterized by only this phase, indicating that the dehydrogenation was fully completed up to this temperature. The relative amount of the two hydride phases and Mg in the different desorbed states can be quantified from the total XRD

peak areas corresponding to the individual phases [52]. It is noted that the oxide content was excluded in this analysis. The variation of phase composition as a function of the dehydrogenation temperature is displayed in Figure 8. Accordingly, the as-milled  $\text{MgH}_2/\text{FeTi}$  (3 h) powder contains eighty volume percent of  $\alpha\text{-MgH}_2$  and 20%  $\gamma\text{-MgH}_2$ . It is evidently confirmed from the pattern that the  $T_1$  transformation corresponds to the desorption of  $\gamma\text{-MgH}_2$ , while during the second endothermic reaction  $\alpha\text{-MgH}_2$  transforms into Mg. The fully desorbed state ( $T = 800$  K) contains only elemental Mg, confirming the perfect and complete hydrogen desorption of the  $\text{MgH}_2/\text{FeTi}$  material.

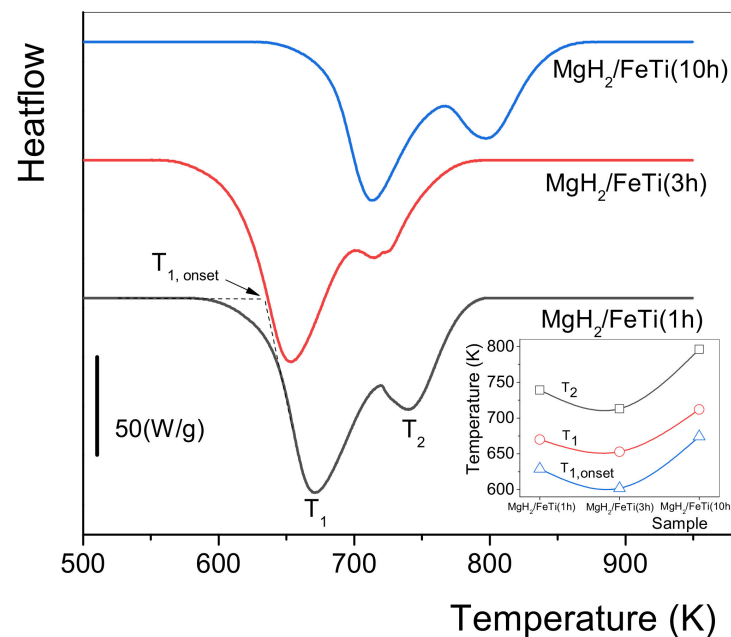


**Figure 6.** Linear heating DSC scans for  $\text{MgH}_2/\text{FeTi}$  powders. The inset shows the variation of the characteristic temperatures for the different composites.

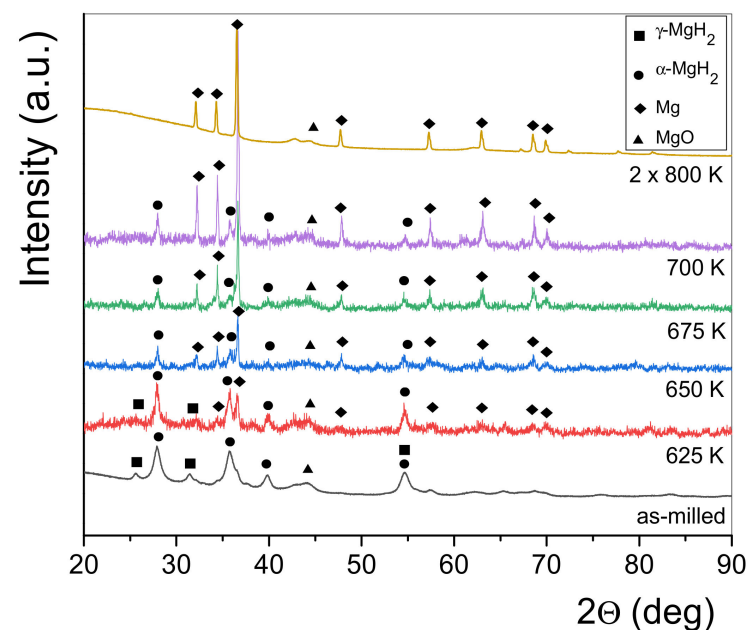


**Figure 7.** Series of XRD patterns of the  $\text{MgH}_2/\text{FeTi}$  (3 h) powder obtained after linear heating up to the designated temperatures.



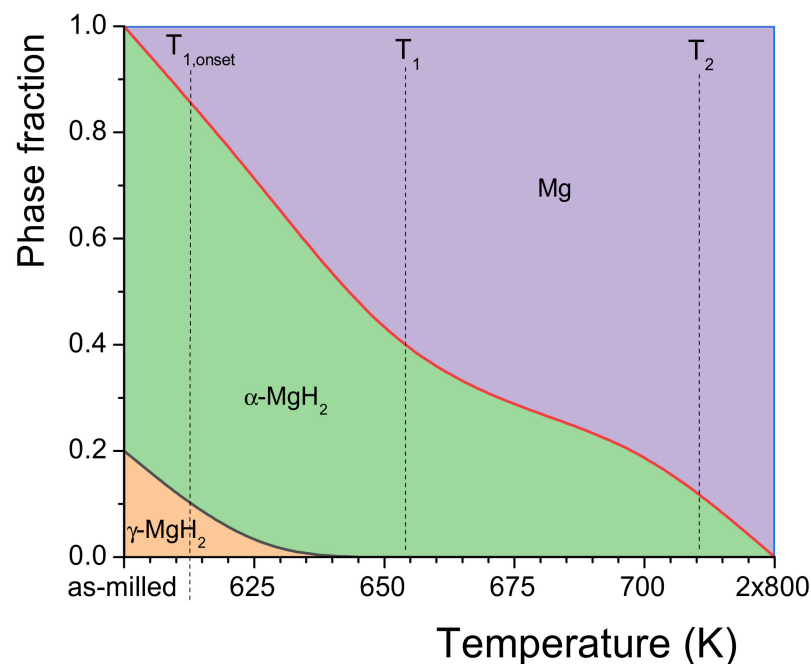


**Figure 8.** Phase evolution during dehydrogenation of the  $\text{MgH}_2/\text{FeTi}$  (3 h) composite powder.

The results of the hydrogenation performance of the  $\text{MgH}_2/\text{FeTi}$  composites can be seen in Figure 9. As seen, all powders can take up a significant amount of hydrogen in a reasonably short time (Figure 9a). According to Table 1, the  $\text{MgH}_2/\text{FeTi}$  (3 h) alloy exhibits outstanding capacity, as it can absorb a total amount of 6.9 wt.% hydrogen. In addition, the 5.2 wt.% absorbed  $\text{H}_2$  in the first 10 min of hydrogenation confirms the excellent kinetics of this material. As also listed in Table 1, the kinetics of the other two powders are worse, i.e.,  $\text{MgH}_2/\text{FeTi}$  (1 h) and  $\text{MgH}_2/\text{FeTi}$  (10 h) can take up only 2.5 wt.% and 1.2 wt.%  $\text{H}_2$  in the first 10 min, respectively, while their total hydrogen uptake is also somewhat lower. As seen in Figure 9b, desorption is complete for all powders, similarly to the dehydrogenation during linear heating in the DSC (see Figures 6 and 7). Despite the exceptional absorption kinetics of  $\text{MgH}_2/\text{FeTi}$  (3 h) powder, its dehydrogenation kinetics performance is somewhat poorer, releasing 2.8 wt.%  $\text{H}_2$  in 10 min. It is also evident from Figure 9b and Table 1 that the longest HEBM time results in the poorest overall dehydrogenation characteristics, despite the rather similar morphology (see Figure 2) and microstructural parameters of the  $\text{MgH}_2/\text{FeTi}$  powders (Figure 5). It is noted that these hydrogenation/dehydrogenation kinetic measurements correspond to the third full cycle for all samples, which presents only a slightly better overall performance compared to the second run. These results may confirm the cycling stability of this system at least for small cycling numbers.

In order to determine the governing mechanism of the hydrogenation and dehydrogenation of the  $\text{MgH}_2/\text{FeTi}$  composites, the normalized  $\alpha(t)$  absorption and desorption kinetic curves were fitted with different model functions. Accordingly, all kinetic data can satisfactorily be fitted by the Johnson–Mehl–Avrami (JMA) function:

$$\alpha(t) = 1 - e^{-kt^n} \quad (2)$$

where  $k$  is a temperature-dependent reaction constant and  $n$  relates to the growth dimensionality of a nucleating phase [53]. For a better visualization, Equation (2) can be transformed into the following expression:

$$\ln(-\ln(1 - \alpha)) = n \cdot \ln(t) + \ln(k) \quad (3)$$

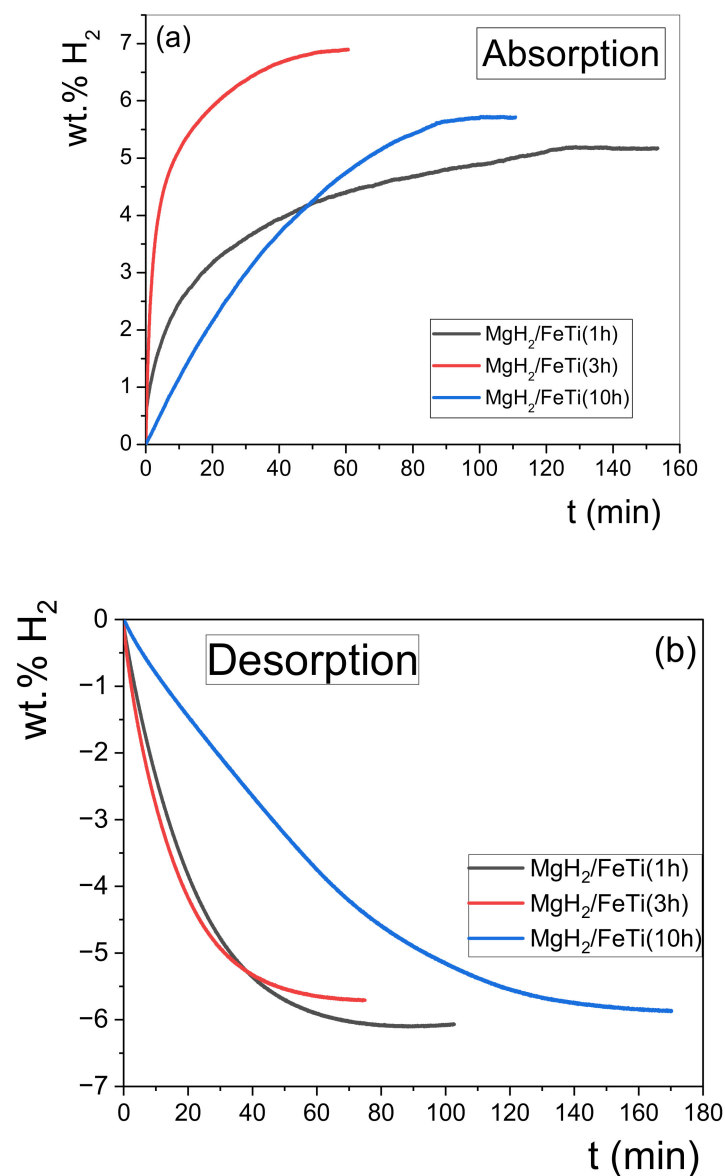


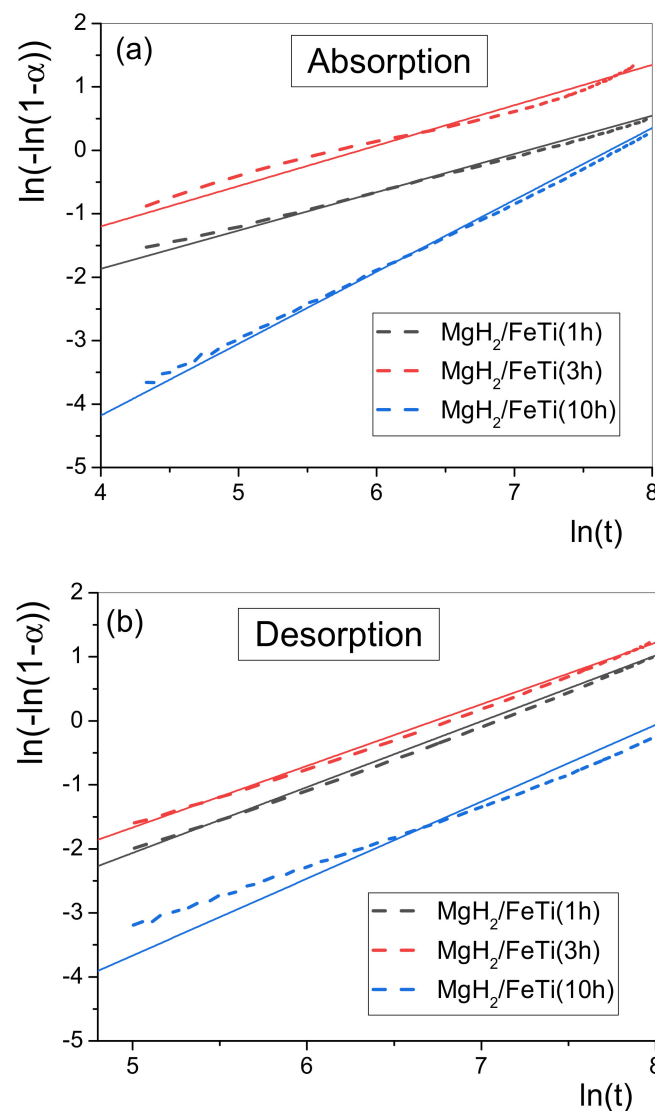
Figure 9. (a) Hydrogenation and (b) dehydrogenation curves obtained for the MgH<sub>2</sub>/FeTi composites.

Table 1. Hydrogen absorption and desorption data for the MgH<sub>2</sub>/FeTi powders.

Sample	Total Absorbed Hydrogen (wt.%)	Absorbed Hydrogen at 10 min (wt.%)	Total Desorbed Hydrogen (wt.%)	Desorbed Hydrogen at 10 min (wt.%)
MgH <sub>2</sub> /FeTi (1 h)	5.2	2.5	6.1	2.3
MgH <sub>2</sub> /FeTi (3 h)	6.9	5.2	5.7	2.8
MgH <sub>2</sub> /FeTi (10)	5.7	1.2	5.9	0.8

Accordingly, the  $\ln(-\ln(1 - \alpha))$  vs.  $\ln(t)$  plot should be a straight line, whose slope provides  $n$ , while the intercept gives  $\ln(k)$ . Such transformed functions can be seen in Figure 10 for all MgH<sub>2</sub>/FeTi powders. In general, the transformed absorption functions follow the linear behavior well (Figure 10a), therefore the entire hydrogenation process can be described by a single JMA exponent, and the fitted values are listed in Table 2. Similarly, the transformed desorption functions for the MgH<sub>2</sub>/FeTi (1 h) and MgH<sub>2</sub>/FeTi (3 h) samples obey a linear relationship (Figure 10b), however, a substantial deviation from the straight line is observed for the MgH<sub>2</sub>/FeTi (10 h) powder at the early stage of

desorption. This behavior corresponds to a slight change in the  $n$  parameter throughout the dehydrogenation process.



**Figure 10.** Double logarithm JMA plots for (a) absorption and (b) desorption of the  $\text{MgH}_2/\text{FeTi}$  powders.

**Table 2.** Hydrogen absorption and desorption constants obtained from the JMA fits of the normalized kinetic curves.

Sample	JMA Absorption Reaction Constant $[k] \text{ (s}^{-1}\text{)}$	JMA Absorption Exponent $[n]$	JMA Desorption Reaction Constant $[k] \text{ (s}^{-1}\text{)}$	JMA Desorption Exponent $[n]$
$\text{MgH}_2/\text{FeTi}$ (1 h)	$7.9 \times 10^{-4}$	0.66	$8.52 \times 10^{-4}$	1.08
$\text{MgH}_2/\text{FeTi}$ (3 h)	$29.6 \times 10^{-4}$	0.58	$11.20 \times 10^{-4}$	0.98
$\text{MgH}_2/\text{FeTi}$ (10 h)	$89.0 \times 10^{-4}$	2.37	$2.91 \times 10^{-4}$	1.32

As seen from Table 1, the  $n$  parameters describing absorption and desorption of the  $\text{MgH}_2/\text{FeTi}$  (1 h) and  $\text{MgH}_2/\text{FeTi}$  (3 h) samples are rather similar, however, the obtained values are anomalously lower than the usual values describing a JMA-type transformation. According to the thorough book of J.W. Christian, these kinetics can be interpreted as a specific type of diffusion-controlled phase growth when precipitates of the nucleating phase ( $\text{MgH}_2$  for absorption and  $\text{Mg}$  for desorption) commence near lattice defects (vacancies and

dislocation), in correlation with the obtained very high value of dislocation density [53]. On the other hand, the  $n$  value for the  $\text{MgH}_2/\text{FeTi}$  (10 h) powder is definitely larger (2.37 for absorption and 1.32 for desorption) which corresponds to a different sorption mechanism, which incorporates several distinct processes, such as diffusion-controlled growth with decreasing nucleation rate and nucleation in the vicinity of lattice defects [53].

#### 4. Conclusions

HEBM was applied to synthesize nanocrystalline  $\text{MgH}_2$  powder samples catalyzed by 10 wt.%  $\text{Fe}_2\text{Ti}$ . Scanning electron microscopy experiments confirmed that  $\text{FeTi}$  catalyst particles are homogeneously dispersed among the hydride agglomerates or pressed into their surface. The XRD patterns of the  $\text{MgH}_2/\text{FeTi}$  composites are dominated by the reflections of tetragonal  $\alpha\text{-MgH}_2$ , however, the high-pressure  $\gamma\text{-MgH}_2$  phase is also present. The recorded diffraction profiles have been evaluated by the CMWP fitting algorithm, in order to determine microstructural parameters of the composite, such as average crystallite size and average dislocation density. The  $D$  values of the two hydride phases are practically independent from the milling time (7–12 nm), while the obtained dislocation density reaches remarkable high values ( $\rho \sim 10^{15} \text{ m}^{-2}$ ). It was obtained from DSC experiments that there exists an optimal milling time (3 h) when desorption occurs at the lowest temperature. XRD of partially dehydrided states confirmed that the two-step endothermic calorimetric event corresponds to the subsequent desorption of  $\gamma\text{-MgH}_2$  and  $\alpha\text{-MgH}_2$ . The best overall hydrogenation performance was obtained for the composite milled for 3 h, with a maximum of 6.9 wt.% absorbed hydrogen. By analyzing the normalized sorption measurements, it was found that all kinetic data can satisfactorily be fitted by the JMA function. The anomalously low JMA exponent suggests that these kinetics can be interpreted as a specific type of diffusion-controlled phase growth when precipitates of the nucleating phase commence near lattice defects.

**Author Contributions:** Calorimetry, X-ray diffraction, writing, editing, Á.R.; powder processing, scanning electron microscopy, R.P.; hydrogen kinetic measurements, T.S.; CMWP analysis, writing, M.G. All authors have read and agreed to the published version of the manuscript.

**Funding:** This research received no external funding.

**Acknowledgments:** R.P. is grateful for the Tempus Organization providing a Stipendium Hungaricum Ph.D. scholarship.

**Conflicts of Interest:** The authors declare no conflict of interest. The funders had no role in the design of the study; in the collection, analyses or interpretation of data; in the writing of the manuscript; or in the decision to publish the results.

#### References

1. International Energy Agency. Key World Energy Statistics 2020. Available online: <https://www.iea.org/reports/key-world-energy-statistics-2020> (accessed on 10 January 2023).
2. Abe, J.; Popoola, P.; Ajenifuja, E.; Popoola, O. Hydrogen energy, economy, and storage: Review and recommendation. *Int. J. Hydrogen Energy* **2019**, *44*, 15072–15086. [CrossRef]
3. Jackson, R.B.; Friedlingstein, P. Persistent fossil fuel growth threatens the Paris Agreement and planetary health. *Environ. Res. Lett.* **2019**, *14*, 12001. [CrossRef]
4. Abdalla, A.M.; Hossain, S.; Nisfindy, O.B.; Azad, A.T.; Dawood, M.; Azad, A.K. Hydrogen Production, Storage, Transportation and Key Challenges with Applications: A Review. *Energy Convers. Manag.* **2018**, *165*, 602–627. [CrossRef]
5. Schlabach, L.; Zuttel, A. Hydrogen-Storage Materials for Mobile Applications. *Nature* **2001**, *414*, 353–358. [CrossRef] [PubMed]
6. Von Colbe, J.B.; Ares, J.-R.; Barale, J.; Baricco, M.; Buckley, C.; Capurso, G.; Gallandat, N.; Grant, D.M.; Guzik, M.N.; Jacob, I.; et al. Application of hydrides in hydrogen storage and compression: Achievements, outlook and perspectives. *Int. J. Hydrogen Energy* **2019**, *44*, 7780–7808. [CrossRef]
7. Hirscher, M.; Yartys, V.A.; Baricco, M.; Bellosta von Colbe, J.; Blanchard, D.; Bowman, R.C.; Broom, D.P.; Buckley, C.E.; Chang, F.; Chen, P.; et al. Materials for hydrogen-based energy storage-past, recent progress and future outlook. *J. Alloys Compd.* **2020**, *827*, 153548. [CrossRef]
8. Lin, H.-J.; Lu, Y.-S.; Zhang, L.-T.; Liu, H.-Z.; Edalati, K.; Révész, Á. Recent Advances in Metastable Alloys for Hydrogen Storage: A Review. *Rare Met.* **2022**, *41*, 1797–1817. [CrossRef]

9. Crivello, J.-C.; Dam, B.; Denys, R.V.; Dornheim, M.; Grant, D.M.; Huot, J.; Jensen, T.R.; de Jongh, P.; Latroche, M.; Milanese, C.; et al. Review of Magnesium Hydride-Based Materials: Development and Optimisation. *Appl. Phys. A* **2016**, *122*, 97. [\[CrossRef\]](#)
10. Révész, Á.; Gajdics, M. Improved H-Storage Performance of Novel Mg-Based Nanocomposites Prepared by High-Energy Ball Milling: A Review. *Energies* **2021**, *14*, 6400. [\[CrossRef\]](#)
11. Aguey-Zinsou, K.-F.; Ares-Fernández, J.-R. Hydrogen in Magnesium: New Perspectives toward Functional Stores. *Energy Environ. Sci.* **2010**, *3*, 526–543. [\[CrossRef\]](#)
12. Pasquini, L. The Effects of Nanostructure on the Hydrogen Sorption Properties of Magnesium-Based Metallic Compounds: A Review. *Crystals* **2018**, *8*, 106. [\[CrossRef\]](#)
13. Suryanarayana, C. Mechanical alloying and milling. *Prog. Mater. Sci.* **2001**, *46*, 1–184. [\[CrossRef\]](#)
14. Zolriasatein, A.; Shokuhfar, A.; Safari, F.; Abdi, N. Comparative study of SPEX and planetary milling methods for the fabrication of complex metallic alloy nanoparticles. *Micro Nano Lett.* **2018**, *13*, 448–451. [\[CrossRef\]](#)
15. Polanski, M.; Bystrzycki, J.; Plocinski, T. The effect of milling conditions on microstructure and hydrogen absorption/desorption properties of magnesium hydride (MgH<sub>2</sub>) without and with Cr<sub>2</sub>O<sub>3</sub> nanoparticles. *Int. J. Hydrogen Energy* **2008**, *33*, 1859–1867. [\[CrossRef\]](#)
16. Sadhasivam, T.; Kim, H.-T.; Jung, S.; Roh, S.-H.; Park, J.-H.; Jung, H.-Y. Dimensional effects of nanostructured Mg/MgH<sub>2</sub> for hydrogen storage applications. *Renew. Sustain. Energy Rev.* **2017**, *72*, 523–534. [\[CrossRef\]](#)
17. Fátay, D.; Révész, Á.; Spassov, T. Particle size and catalytic effect on the dehydrogenation of MgH<sub>2</sub>. *J. Alloys Compd.* **2005**, *399*, 237–241. [\[CrossRef\]](#)
18. Fátay, D.; Spassov, T.; Delchev, P.; Ribárik, G.; Révész, Á. Microstructural development in nanocrystalline MgH<sub>2</sub> during H-absorption/desorption cycling. *Int. J. Hydrogen Energy* **2007**, *32*, 2914–2919. [\[CrossRef\]](#)
19. Novakovic, J.G.; Novakovic, N.; Kurko, S.; Govedarovic, S.M.; Pantic, T.; Mamula, B.P.; Batalovic, K.; Radakovic, J.; Rmus, J.; Shelyapina, M.; et al. Influence of defects on the stability and hydrogen-sorption behavior of Mg-based hydrides. *Chem. Phys. Chem.* **2019**, *20*, 1216–1247. [\[CrossRef\]](#)
20. Révész, Á.; Kánya, Z.; Verebelyi, T.; Szabó, P.J.; Zhilyaev, A.P.; Spassov, T. The effect of high-pressure torsion on the microstructure and hydrogen absorption kinetics of ball-milled Mg<sub>70</sub>Ni<sub>30</sub>. *J. Alloys Compd.* **2010**, *504*, 83–88. [\[CrossRef\]](#)
21. Khan, D.; Zou, J.; Zeng, X.; Ding, W. Hydrogen storage properties of nanocrystalline Mg<sub>2</sub>Ni prepared from compressed 2MgH<sub>2</sub>-Ni powder. *Int. J. Hydrogen Energy* **2018**, *43*, 22391–22400. [\[CrossRef\]](#)
22. House, S.D.; Vajo, J.J.; Ren, C.; Zaluzec, N.J.; Rockett, A.A.; Robertson, I.M. Impact of Initial Catalyst Form on the 3D Structure and Performance of Ball-Milled Ni-Catalyzed MgH<sub>2</sub> for Hydrogen Storage. *Int. J. Hydrogen Energy* **2017**, *42*, 5177–5187. [\[CrossRef\]](#)
23. Zhang, Q.; Zang, L.; Huang, Y.; Gao, P.; Jiao, L.; Yuan, H.; Wang, Y. Improved hydrogen storage properties of MgH<sub>2</sub> with Ni-based compounds. *Int. J. Hydrogen Energy* **2017**, *42*, 24247–24255. [\[CrossRef\]](#)
24. Antikeira, F.J.; Leiva, D.R.; Zepon, G.; de Cunha, B.F.R.F.; Figueroa, S.J.A.; Botta, W.J. Fast Hydrogen Absorption/Desorption Kinetics in Reactive Milled Mg-8 Mol% Fe Nanocomposites. *Int. J. Hydrogen Energy* **2020**, *45*, 12408–12418. [\[CrossRef\]](#)
25. Révész, Á.; Gajdics, M.; Spassov, T. Microstructural evolution of ball-milled Mg-Ni powder during hydrogen sorption. *Int. J. Hydrogen Energy* **2013**, *38*, 8342–8349. [\[CrossRef\]](#)
26. Song, M.Y.; Kwon, I.H.; Kwon, S.N.; Park, C.G.; Park, H.R.; Bae, J.-S. Preparation of hydrogen-storage alloy Mg-10wt% Fe<sub>2</sub>O<sub>3</sub> under various milling conditions. *Int. J. Hydrogen Energy* **2006**, *31*, 43–47. [\[CrossRef\]](#)
27. Ma, Z.; Liu, J.; Zhu, Y.; Zhao, Y.; Lin, H.; Zhang, Y.; Li, H.; Zhang, J.; Liu, Y.; Gao, W.; et al. Crystal-Facet-Dependent Catalysis of Anatase TiO<sub>2</sub> on Hydrogen Storage of MgH<sub>2</sub>. *J. Alloys Compd.* **2020**, *822*, 153553. [\[CrossRef\]](#)
28. Zhang, M.; Xiao, X.; Wang, X.; Chen, M.; Lu, Y.; Liu, M.; Chen, L. Excellent Catalysis of TiO<sub>2</sub> Nanosheets with High-Surface-Energy {001} Facets on the Hydrogen Storage Properties of MgH<sub>2</sub>. *Nanoscale* **2019**, *11*, 7465–7473. [\[CrossRef\]](#)
29. Barkhordarian, G.; Klassen, T.; Bormann, R. Fast hydrogen sorption kinetics of nanocrystalline Mg using Nb<sub>2</sub>O<sub>5</sub> as catalyst. *Scr. Mater.* **2003**, *49*, 213–217. [\[CrossRef\]](#)
30. Ruse, E.; Buzaglo, M.; Pevzner, S.; Pri-Bar, I.; Skripnyuk, V.M.; Rabkin, E.; Regev, O. Tuning Mg hydriding kinetics with nanocarbons. *J. Alloys Compd.* **2017**, *725*, 616–622. [\[CrossRef\]](#)
31. Zhang, X.; Leng, Z.; Gao, M.; Hu, J.; Du, F.; Yao, J.; Pan, H.; Liu, Y. Enhanced hydrogen storage properties of MgH<sub>2</sub> catalyzed with carbon-supported nanocrystalline TiO<sub>2</sub>. *J. Power Source* **2018**, *398*, 183–192. [\[CrossRef\]](#)
32. Gajdics, M.; Spassov, T.; Kis, V.K.; Schafner, E.; Révész, Á. Microstructural and Morphological Investigations on Mg-Nb<sub>2</sub>O<sub>5</sub>-CNT Nanocomposites Processed by High-Pressure Torsion for Hydrogen Storage Applications. *Int. J. Hydrogen Energy* **2020**, *45*, 7917–7928. [\[CrossRef\]](#)
33. Guoxian, L.; Erde, W.; Shoushi, F. Hydrogen absorption and desorption characteristics of mechanically milled Mg-35wt.% FeTi<sub>1.2</sub> powders. *J. Alloys Compd.* **1995**, *223*, 111–114. [\[CrossRef\]](#)
34. Neto, R.M.L.; de Araújo Silva, R.; Floriano, R.; Coutinho, G.C.S.; Falcão, R.B.; Leiva, D.R.; Botta Filho, W.J. Synthesis by High-Energy Ball Milling of MgH<sub>2</sub>-TiFe Composites for Hydrogen Storage. *Mater. Sci. Forum* **2017**, *899*, 13–18. [\[CrossRef\]](#)
35. Silva, R.; Lean Neto, R.L.; Leiva, D.R.; Ishikawa, Kiminami, C.S.; Jorge, A.M., Jr.; Botta, W.J. Room temperature hydrogen absorption by Mg and Mg TiFe nanocomposites processed by high-energy ball milling. *Int. J. Hydrogen Energy* **2018**, *43*, 12251–12259. [\[CrossRef\]](#)
36. Kondo, T.; Shindo, K.; Sakurai, Y. Dependence of hydrogen storage characteristics of Mg-TiFe<sub>0.92</sub>Mn<sub>0.08</sub> composite on amount of TiFe<sub>0.92</sub>Mn<sub>0.08</sub>. *J. Alloys Compd.* **2005**, *404*, 511–514. [\[CrossRef\]](#)



37. Chen, B.-H.; Kuo, C.-H.; Ku, J.-R.; Yan, P.-S.; Huang, C.-J.; Jeng, M.-S.; Tasu, F.-H. Highly improved with hydrogen storage capacity and fast kinetics in Mg-based nanocomposites by CNTs. *J. Alloys Compd.* **2013**, *568*, 78–83. [\[CrossRef\]](#)
38. Bassetti, A.; Bonetti, E.; Pasquini, L.; Montone, A.; Grbovic, J.; Antisari, V. Hydrogen desorption from ball milled MgH<sub>2</sub> catalyzed with Fe. *Eur. Phys. J. B* **2005**, *43*, 19–27. [\[CrossRef\]](#)
39. Ulate-Kolitsky, E.; Tougas, B.; Neumann, B.; Schade, C.; Huot, J. First hydrogenation of mechanically processed TiFe-based alloy synthesized by gas atomization. *Int. J. Hydrogen Energy* **2021**, *46*, 7381–7389. [\[CrossRef\]](#)
40. Patel, A.K.; Duguay, A.; Tougas, B.; Schade, C.; Sharma, P.; Huot, J. Microstructure and first hydrogenation properties of TiFe alloy with Zr and Mn as additives. *Int. J. Hydrogen Energy* **2020**, *45*, 787–797. [\[CrossRef\]](#)
41. Gosselin, C.; Huot, J. First Hydrogenation Enhancement in TiFe Alloys for Hydrogen Storage Doped with Yttrium. *Metals* **2019**, *9*, 242. [\[CrossRef\]](#)
42. Gosselin, C.; Huot, J. Hydrogenation Properties of TiFe Doped with Zirconium. *Materials* **2015**, *8*, 7864–7872. [\[CrossRef\]](#) [\[PubMed\]](#)
43. Falcão, R.B.; Dammann, E.D.; Rocha, C.J.; Durazzo, M.; Ichikawa, R.U.; Martinez, L.G.; Botta, W.J.; Neto, R.M.L. An alternative route to produce easily activated nanocrystalline TiFe powder. *Int. J. Hydrogen Energy* **2018**, *43*, 16107–16116. [\[CrossRef\]](#)
44. Edalati, K.; Matsuda, J.; Arita, M.; Daio, T.; Akiba, E.; Horita, Z. Mechanism of activation of TiFe intermetallics for hydrogen storage by severe plastic deformation using high-pressure torsion. *Appl. Phys. Lett.* **2013**, *103*, 143902. [\[CrossRef\]](#)
45. Oliveira, V.B.; Beatrice, C.A.G.; Neto, R.M.L.; Silva, W.B.; Pessan, L.A.; Botta, W.J.; Leiva, D.R. Hydrogen Absorption/Desorption Behavior of a Cold-Rolled TiFe Intermetallic Compound. *Mater. Res.* **2021**, *24*, e202102042021. [\[CrossRef\]](#)
46. Edalati, K.; Matsuda, J.; Yanagida, A.; Akiba, E.; Horita, Z. Activation of TiFe for hydrogen storage by plastic deformation using groove rolling and high-pressure torsion: Similarities and differences. *Int. J. Hydrogen Energy* **2014**, *39*, 15589–15594. [\[CrossRef\]](#)
47. Gajdics, M.; Spassov, T.; Kovács Kis, V.; Béke, F.; Novák, Z.; Schafner, E.; Révész, Á. Microstructural Investigation of Nanocrystalline Hydrogen-Storing Mg-Titanate Nanotube Composites Processed by High-Pressure Torsion. *Energies* **2020**, *13*, 563. [\[CrossRef\]](#)
48. Ribárik, G.; Jóni, B.; Ungár, T. Global optimum of microstructure parameters in the CMWP line-profile-analysis method by combining Marquardt-Levenberg and Monte-Carlo procedures. *J. Mater. Sci. Technol.* **2019**, *35*, 1508–1514. [\[CrossRef\]](#)
49. Ribárik, G.; Gubicza, J.; Ungár, T. Correlation between strength and microstructure of ball-milled Al–Mg alloys determined by X-ray diffraction. *Mater. Sci. Eng. A* **2004**, *387*, 343–347. [\[CrossRef\]](#)
50. Révész, Á.; Fátay, D. Microstructural evolution of ball-milled MgH<sub>2</sub> during a complete dehydrogenation–hydrogenation cycle. *J. Power Source* **2010**, *195*, 6997–7002. [\[CrossRef\]](#)
51. Urretavizcaya, G.; García, G.; Serafini, D.; Meyer, G. Mg–Ni alloys for hydrogen storage obtained by ball milling. *Lat. Am. Appl. Res.* **2002**, *32*, 289–294.
52. Gajdics, M.; Calizzi, M.; Pasquini, L.; Schafner, E.; Révész, Á. Characterization of a nanocrystalline Mg–Ni alloy processed by high-pressure torsion during hydrogenation and dehydrogenation. *Int. J. Hydrogen Energy* **2016**, *41*, 9803–9809. [\[CrossRef\]](#)
53. Christian, J.W. *The Theory of Transformations in Metals and Alloys*; Pergamon: Oxford, UK, 1975.

**Disclaimer/Publisher’s Note:** The statements, opinions and data contained in all publications are solely those of the individual author(s) and contributor(s) and not of MDPI and/or the editor(s). MDPI and/or the editor(s) disclaim responsibility for any injury to people or property resulting from any ideas, methods, instructions or products referred to in the content.